Optimization of a squirrel cage fan

Alla Eddine Benchikh Le Hocine, Sébastien Poncet, Hachimi Fellouah
Department of Mechanical Engineering, Université de Sherbrooke
2500 Boul. de l'Université, Sherbrooke (QC) J1K 2R1 Canada
Email: alla.benchikh.le.hocine@USherbrooke.ca

***Abstract*—The restrictions related to air quality are increasing making the improvement of the air system important. The squirrel cage fan (SCF), also known as forward-curved multi-blade centrifugal fan, is widely used in vacuum systems. Most of researches so far used commercial software to study and optimize the SCF. In the present study, a complete automatic optimization process loop is developed based only on open source libraries: Dakota, Salome and OpenFOAM. Up to seven design parameters are selected. The Latin Hypercube Sampling (LHS) method is preferred to determine the design points and then the Kriging and Efficient Global optimization (EGO) metamodels are built. A 3D incompressible simple FOAM solver is coupled to the Multiple reference frame (MRF) approach to model the flow in the SCF. An efficiency improvement of 8.46% is reached by the EGO approach. A strong vortex is observed in the cut-off region. The optimal design is finally validated against the produced prototype, with an error of 3.4% on the efficiency.**

***Index Terms*—Squirrel cage fan, OpenFoam, Dakota, Design of Experiments, Surrogate model, Latin Hypercube Sampling**

I. Introduction

The society is highly concerned and more sensible to the air quality of their outdoor and indoor environments. The COVID-19 pandemy certainly strengthens the researches about the improvement and adaptation of ventilation systems [1]. The improvement of the HVAC (heating, ventilation and air-conditioning) system component efficiency is becoming a necessity to ensure a trade-off between particle captation and power consumption. The squirrel cage fan (SCF) has been extensively used for decades in HVAC systems and other household appliances (bath room, range hood) [2]. The SCF is a special centrifugal fan and also known as forward-curved multi-blade centrifugal fan. In general, the SCF is prone to flow separation around the blades due to their two-dimensional circular arc profile [3], and is also subject to non-uniformity of the flow at the impeller inlet due to the sharp flow direction turning [4], [5]. These flow mechanisms and patterns lead to lower performances of the SCF and the increase of the power consumption [6]. Thus, an improvement of the flow condition inside the SCF is necessary.

Design of experiments (DOE) and metamodels have been used gradually in the optimization process of squirrel cage fans due to their ability to converge towards optimum designs efficiently. Kim and Seo [7] investigated numerically the improvement of the SCF efficiency by studying the effect of cutoff location and radius, and impeller width. The authors coupled numerical calculations and the response surface method (RSM) or also known as metamodels. For the numerical calculations, 3D incompressible RANS simulations were run using the commercial software CFX and the turbulence model k-ε. The flow around the blades and inside the impeller was not modeled to reduce computing time and was calculated by an impeller force model. For the response surface method, the quadratic polynomial model available in the commercial software SPSS was used. Kim and Seo [7] validated their numerical calculations against the experimental data of Kim and Kang [8] by hot-wire probe around the reference SCF design. At the inlet, an acceptable agreement was observed for the axial distribution of the radial velocity component with a maximum error of 20%. The quadratic polynomial model allowed to improve the maximum efficiency and the static pressure coefficient by 38.8% and 1.66%, respectively. Any validation of the obtained optimum design by a metamodel was accomplished by CFD or experimental tests. In a recent study by Zhou et $al.$ [9], the Kriging surrogate model was coupled with CFD to optimize the blade profile for a centrifugal SCF. The authors used the modified Hicks-Henne function to design a simple arc blade, where three amplitude coefficients were selected as input parameters for the optimization process. In their study, only the blade profile function was optimized and the other part of the SCF remained identical. For the numerical calculations, a 3D incompressible RANS approach was used with the turbulence model k-ω SST and the commercial software ANSYS Fluent. A latin hypercube design was employed to obtain the sets of sampling points and the NSGA-II method was used to determine the optimal design from the Kriging response surface. Zhou et $al.$ [9] observed a good agreement between the predicted values by the Kriging model and the CFD with an average relative error of 2.74% and 2.61% for the efficiency and flowrate, respectively. Furthermore, the optimal design improved the efficiency by 4.21% compared to the initial design. The authors validated also their numerical model for the optimal design against experimental data with a maximum error of 3.2% in terms of efficiency.

Most of the published studies that investigated and optimized the SCF focused on the impeller or the volute parameters separately. Also, they used commercial softwares for the CFD calculations and optimization like ANSYS Fluent or CFX [2], [10], [11]. In the current study, full 3D simulations are carried out in order to optimize the efficiency and force applied on the impeller by using only opensource softwares. Different geometrical parameters of the impeller and volute are integrated simultaneously in an optimization loop using the Latin Hypercube Sampling (LHS), CFD and metamodels. The optimization process is also governed by an opensource software named Dakota. The first numerical results obtained by the Design Of Experiment (DOE) method are used to construct a response surface of a Surrogate Based Optimization (SBO, Metamodels). Furthermore, an advanced optimization method named Efficient Global Optimization (EGO) is employed to obtain the best configuration. The numerical performance of the optimal configuration is carefully validated against a new set of experimental data.

II. NUMERICAL MODELING

A 3D steady-state Navier-Stokes incompressible solver has been employed by using the opensource OpenFOAM 6 librairies to model and optimize the SCF performances.

A. Geometrical modelling

Figure 1 shows a 3D sketch of the SCF in Configurations 1 and 2. In both configurations, a Latin Hypercube Sampling (LHS) has been used in the Design of Experiments (DoE) technique. The main difference between both configurations remains in the design of the hub. For Configuration 1, a conical hub is constructed with a diameter and a height of 0.12 m and 0.077 m, respectively. For Configuration 2, the hub corresponds to a cylinder with a diameter and a height of 0.04 m and 0.066 m, respectively. The external diameter (D_2) and the height of the impeller (H_2) are equal to 0.1524 m and 0.0762 m, respectively. The SCF is a 51 bladed fans equipped with 4 digit NACA having a thickness of 2.2 mm.

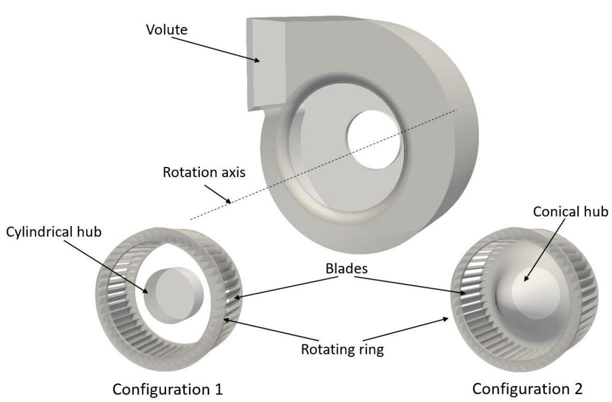

Fig. 1. 3D sketch of the SCF for Configurations 1 and 2.

The SCF is placed in an open environment represented herein by a half sphere with a diameter of $D_{ext} = 1.2\ m$ (Fig.2). The volute is connected to an exit duct with a diameter and length of $D_p = 0.10\ m$ and $L_p = 0.92\ m$, respectively. A transition zone with a length $L_{tr} = 0.051\ m$ is employed to link the volute outlet and the exit duct.

B. Numerical methods

The calculations of the flow dynamics around the SCF are performed by a 3D steady-state incompressible Reynolds averaged Navier-Stokes (RANS) solver named SimpleFoam (OpenFoam 6), which was successfully applied to model the flow around fans and turbines [12]–[14].

A fully second-order scheme is used for the spatial discretization in order to minimize excessive numerical dissipation. The Laplacian and gradient terms are discretized by a bounded Gauss linear numerical scheme. A linear approach is selected for the interpolation scheme. The SIMPLE algorithm enables to overcome the pressure-velocity coupling. The generalized geometric-algebraic multi-grid (GAMG) solver with the combined Diagonal incomplete-Cholesky/Gauss Seidel (symmetric) smoother is selected to solve the pressure. The preconditioned bi-conjugate gradient (PBiCG) solver with Diagonal incomplete-LU (DILU) pre-conditioner is used to solve the rest of the discretized equations.

The turbulent flow is modeled by the $k - \omega$ SST closure developed by Menter [15]. It combines the robust formulation of the $k - \omega$ Wilcox model [16] in the near wall region and the $k - \varepsilon$ away from the wall. Very satisfactory results were obtained by multiple authors when using the $k - \omega$ SST turbulence closure in different fan configurations [17]–[19], and even better results than other two-equation models as the $k - \epsilon$ family [20].

C. Numerical parameters

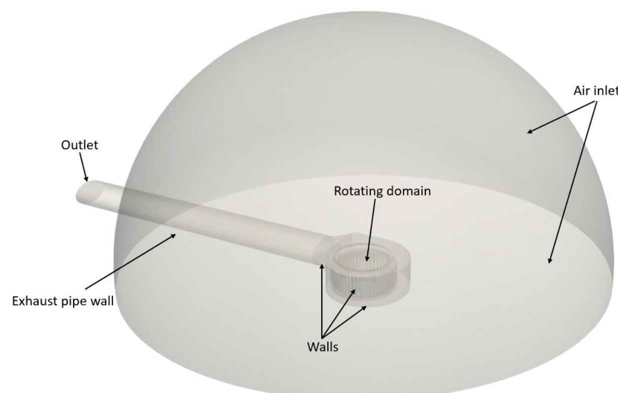

Fig. 2. 3D sketch of the computational domain with the boundary conditions.

The different boundary conditions of the computational domain are shown in Figure 2. Three main regions are defined: the rotor (impeller), the surrounding environment and the volute with the exit pipe. The rotor region lies inside the volute and includes the fan blades, the rotating ring and the hub. The rotor rotating speed is set to 900 rpm. An inlet mass flowrate condition of $0.0588\ kg/s$ (105 cfm) is imposed at the half-sphere surface with a turbulence intensity of 5%. The air parameters are assumed to be constant and evaluated at 293 K. For the impeller, a no slip wall condition is imposed at the blade surfaces, hub, rotating ring and disc plate. The same condition is also applied on the volute and the exit pipe surfaces. A pressure outlet is used at the pipe outlet surface where a static pressure of $24.91\ Pa$ is imposed. The multiple reference frame (MRF) approach is used to model the rotation motion of the rotor region.

Figure 3 shows different views of the unstructured grid mesh generated by the open-source Salome library. The mesh is composed of tetrahedral elements. Ten prismatic layers are generated around the blades with a stretching factor of 1.1. Different mesh refinements with factors equal to 4 and 3 are imposed in the volute and the exit pipe, respectively. The average total number of elements in the whole domain is around 11.7 million cells, with 9 and 2.2 million elements in the rotor and volute regions, respectively. The maximum value of the wall coordinate satisfies the requirement for a low-Reynolds number approach ($y^+ < 0.9$). The selected mesh parameters are obtained based on a mesh convergence study.

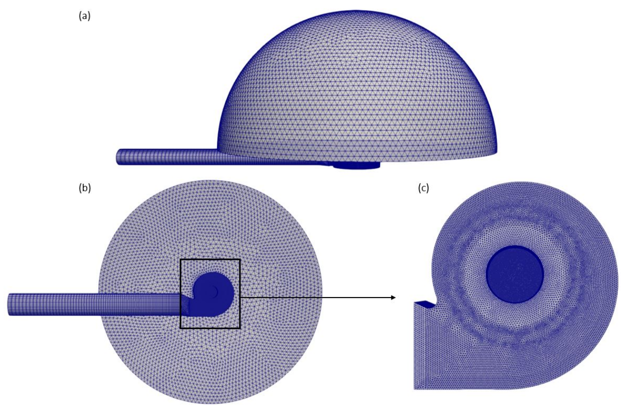

Fig. 3. Views of the mesh distribution: (a) front; (b) rear; (c) lateral.

Each RANS calculation took approximately 1-2 days using 32 processors (AMD Opteron 6172). During all the optimization process, around 4736 processors were used for a total time of 296 days. The convergence is achieved when: (i) the global fan efficiency deviation between two subsequent iterations gets below 0.1%; (ii) all residuals are lower than 10^{-7}; and (iii) the mass imbalance is lower than 10^{-6}. A relaxation factor of 0.3 was used for the velocity components, k and ω.

III. Optimization Process and Methods

A. Optimization loop

The optimization procedure is displayed on Fig.4. Initially, the design space is determined by the selected input parameters and their minimum and maximum bounds. In Configurations 1 and 2, five input parameters are selected, while in Configuration 3, two more design parameters are added to expand the design space of Configuration 2. The input variables are:

1) D_1/D_2 is the ratio between the wheel interior diameter and the wheel external diameter;
2) β_1 is the blade leading edge angle (angle of attack);
3) β_2 is the blade trailing edge angle (outlet angle);
4) R_c/D_2 is the ratio between the cutoff radial position and the wheel external diameter;
5) θ_c is the cut-off angular position;
6) D_2 is the wheel external diameter;
7) r_c/D_2 is the ratio between the cutoff radius and the wheel external diameter.

The different input variables are introduced in Dakota and a DOE is conducted by using LHS. The LHS is a stratified

TABLE I
Design parameters with lower and upper bounds of the design space.

Design parameters	lower bound	upper bound
D_1/D_2 [-]	0.8	0.9
β_1 [°]	85	110
β_2 [°]	25	35
R_c/D_2 [-]	0.556	0.620
θ_c [°]	-35	-10
D_2 [m]	0.1524	0.1587
r_c/D_2 [-]	0.05	0.065

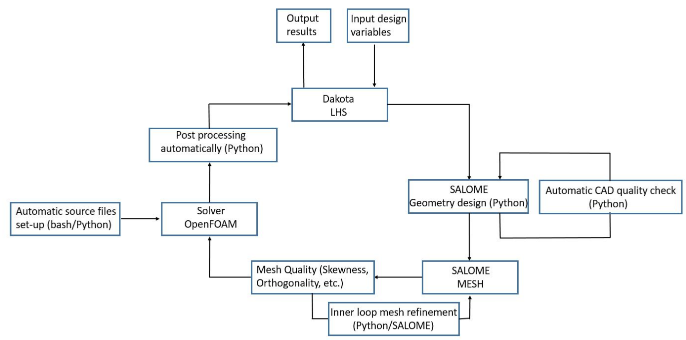

Fig. 4. Optimization loop process for the LHS method.

sampling method where the uncertain variable range is divided into N parts (segments) with equal probability. A random sample is selected from each of the equal probability segments. The N values for each of the selected parameters are combined in a shuffling operation to construct a set of N parameter vectors with a specified correlation structure. The LHS method has the advantage to require fewer samples than the traditional Monte-Carlo method for the same accuracy in statistics.

As the LHS technique is run by Dakota, a set of input parameters variables are defined. In the next step, Salome is loaded and the entire computational domain is created automatically based on Python scripts. As the geometry is constructed, a Python script is used to check any irregularity in the geometry. In the next step, the Salome mesh library is used and a Python script with all the mesh parameters is executed in order to generate the unstructured mesh. A CheckMesh function of OpenFOAM is used in order to ensure the mesh quality. After, all the calculations are run simultaneously on a cluster. Once accomplished, a post-processing is executed to extract the objective functions herein: the global efficiency and the forces applied on the impeller.

B. Metamodel approach

The optimal design obtained by the LHS method represents the best configuration over limited design points. In order to explore the entire design space and to confirm or find another optimal design, a metamodel (Surrogate-Based Optimization SBO) has to be constructed. The metamodel construction process is displayed in Fig.5. Multiple surrogate models are used in the design optimization such as radial basis functions, polynomial regression, neural networks, etc. In this study,

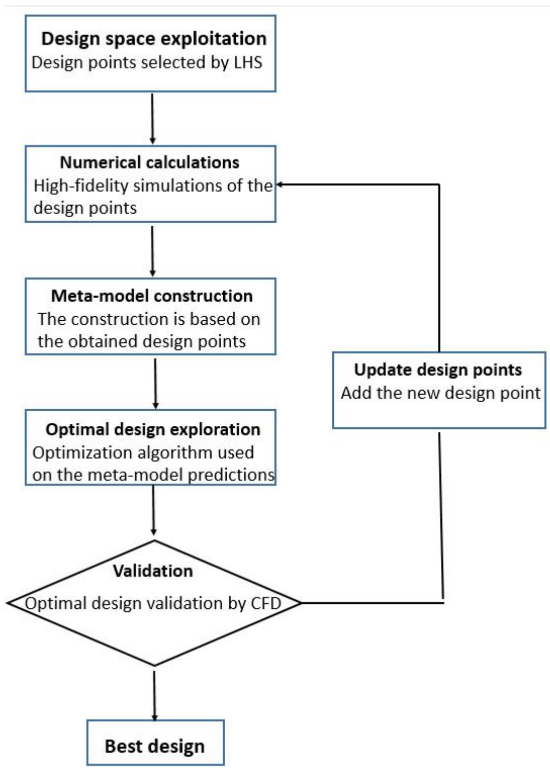

Fig. 5. Metamodel (surrogate based) optimization workflow.

the Kriging metamodel is selected to its ability to predict accurately the efficiency on axial and centrifugal fans [21] and to model different function typologies. The Kriging surrogate (Gaussian process) is based on the achievement of a Gaussian stochastic process to the modeled objective functions. Mathematically, the Kriging function prediction at a point (design parameter) x is defined as:

$$\hat{f}(x) = \hat{\mu} + \psi R^{-1}(Y - 1\hat{\mu}) \tag{1}$$

where $\hat{\mu}$ is the maximum likelihood estimator of the random field mean and $\hat{f}(x)$ is the predicted objective (response) function for the variable x. Y represents a set with a dimension N of the calculated data and is expressed as follows:

$$Y = [f(x^{(i)})...f(x^{(N)})] \tag{2}$$

$f(x)$ represents the value obtained by CFD at the design points (x) selected by the LHS method. ψ in Eq.1 is a vector with a length N representing the basis functions. The basis functions ψ are weighted by the term $R^{-1}(Y - 1\hat{\mu})$, where R is the $N \times N$ correlations matrix among the design points.

In addition to the different metamodels, the efficient global optimization (EGO) method is also applied to predict the objective functions. The EGO has been developed by Jones et $al.$ [22] and is based on the Kriging metamodel. The EGO model contrary to the surrogate model has the ability to select the next sample point with the maximum probability that the global minimum exists in the design space. The probability is defined as an expected improvement (EI) function:

$$E(I(x)) = \left(f_{min} - \hat{f}\right)\Phi\left(\frac{f_{min} - \hat{f}}{s}\right) + s\phi\left(\frac{f_{min} - \hat{f}}{s}\right) \tag{3}$$

where f_{min} is the obtained minimum value from the CFD calculations, $\hat{f}$ is the predicted value by the Kriging model. The parameter s is the standard error at x. $\phi(.)$ and $\Phi()$ are the standard normal density and distribution function, respectively. $I(x)$ is the improvement at the point x defined as:

$$I(x) = max\left[(f_{min} - \hat{f}(x)), 0\right] \tag{4}$$

The iterative process will continue until a global minimum is found and validated against the CFD results. A convergence tolerance of 10^{-2} is selected for the efficiency and the force applied on the wheel. Contrary to standard metamodels, the EGO approach needs more computational resources to converge toward an optimal design.

IV. Results and Discussion

In this section, the results of the optimization process by using LHS and metamodels are presented for the three configurations.

A. Performance comparison

The optimal value of the efficiency and F_{xy} are determined after completing all the optimization process for the LHS approach and constructing the surrogate models according to the charts displayed in Figures 4 and 5. The optimization objective is to minimize F_{xy} in order to avoid any mechanical damage and to maximize the SCF efficiency.

All the predicted values of the objective functions by the different methods are presented in Table II. In Configuration 1, the Kriging model predicts with accuracy the efficiency and F_{xy} values with errors of 2.16% and 8.4%, respectively. The major source of error is essentially due to its limitation in complex responses, where the flow is highly turbulent with 3D vortices interacting with the impeller blades. The application of the EGO based on the Kriging metamodel allows the improvement of the efficiency and F_{xy} by 2.35% and 5.71%, respectively, compared to the optimal LHS design. The EGO method converges after 10 iterations. As the design space is expanded by the EGO approach compared to the Kriging, the probability to find an optimal design which meets the objective function requirements is increased. In Configuration 2, by using the Kriging model and EGO, the initial optimal design obtained by the LHS is improved in a short time and few calculation resources with an improvement of 2.63% and 28.45% for the efficiency and F_{xy}, respectively. As in Configuration 1, the optimal design with the EGO model improves the objective functions specifically F_{xy} by 11.49% compared to the Kriging model validation. In Configuration 3, the Kriging model provides an accurate prediction with errors of 1.13% and 8.15% for the efficiency and F_{xy}, respectively. The EGO

TABLE II
SUMMARY OF THE PREDICTED OBJECTIVE FUNCTION VALUES BY THE DIFFERENT MODELS FOR THE THREE CONFIGURATIONS.

Configurations	Method	D_1/D_2 [-]	β_1 [°]	β_2 [°]	r_c/D_2 [-]	θ_c [°]	D_2 [m]	R_c/D_2 [-]	Efficiency [%]	F_{xy} [N]
Conf.1	LHS	0.866	89.602	25.436	0.567	-27.413	/	/	45.59	0.298
	Kriging	0.845	104.787	25.154	0.559	-19.566	/	/	47.64 (3.36%)	0.263 (8.4%)
	OF validation	0.845	104.787	25.154	0.559	-19.566	/	/	44.28	0.241
	EGO	0.838	87.772	25.002	0.556	-29.995	/	/	47.94	0.281
Conf.2	LHS	0.824	105.459	25.376	0.580	-16.166	/	/	47.35	0.355
	Kriging	0.845	104.787	25.154	0.559	-19.566	/	/	51.51 (2.11%)	0.294 (2.38%)
	OF validation	0.845	104.787	25.154	0.559	-19.566	/	/	49.40	0.287
	EGO	0.841	109.998	25.002	0.556	-19.995	/	/	49.98	0.254
Conf.3	LHS	0.849	96.245	25.524	0.567	-21.294	0.1528	0.0563	49.83	0.226
	Kriging	0.869	103.102	25.801	0.564	-16.358	0.1559	0.0549	51.91 (1.13%)	0.233 (8.15%)
	OF validation	0.869	103.102	25.801	0.564	-16.358	0.1559	0.0549	50.78	0.252
	EGO	0.843	98.837	25.020	0.556	-29.958	0.1524	0.0649	54.05	0.275

model provides an optimal design with an improvement of the efficiency by 3.27% and 4.22% compared to the Kriging OpenFOAM (OF) validation and LHS, respectively.

B. Mean flow field

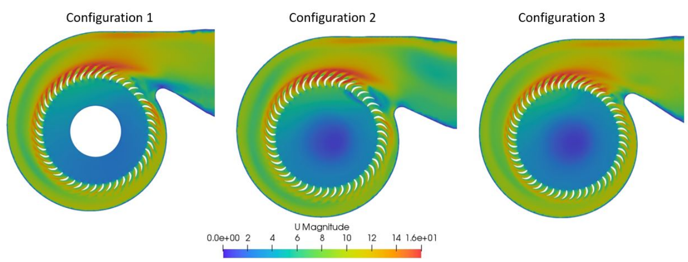

Fig. 6. Distribution of the mean velocity magnitude U (m/s) on plane 1 ($x = 0$, $y = 0$,$z = H_2/2$) for Configurations 1, 2 and 3.

Figure 6 displays the 2D contours of the mean velocity magnitude U (m/s) on plane 1. Plane 1 is located at the mid-span of the SCF ($x = 0$, $y = 0$,$z = H_2/2$). For Configurations 1 and 2, a flow separation is observed on the leading edge of multiple blades located toward the outlet (transition), followed by a flow acceleration near the trailing edge region. The flow acceleration region is also observed in Configuration 3. This acceleration is mainly due to the rotating acceleration by the impeller. Near the cut-off, a recirculation region is observed for Configuration 1. However, in Configuration 2, the recirculation region is shifted near the blades. The displacement of the recirculation region is due to the narrower cut-off angle and larger exit surface. In Configuration 3, a small recirculation is observed near the cut-off region. In the hub region, all the configurations show a comparable U distribution.

To confirm the flow separation around the blades and near the cut-off, the relative total pressure (Pa) is investigated in plane 1 on Fig.7. The relative total pressure is obtained by subtracting the atmospheric pressure at the ambient conditions. The total pressure distributions for Configurations 1 and 2 confirm the observed vortex in Figs 6. The negative spot between the cut-off and the blades in the exit region represents the strong vortex rotating motion. However, in Configuration 3, the negative spot is significantly reduced due to the wide and small cut-off angle and radial position, respectively. Furthermore, the flow around the blades in Configuration 1 is mostly attached except near the upper region where a flow

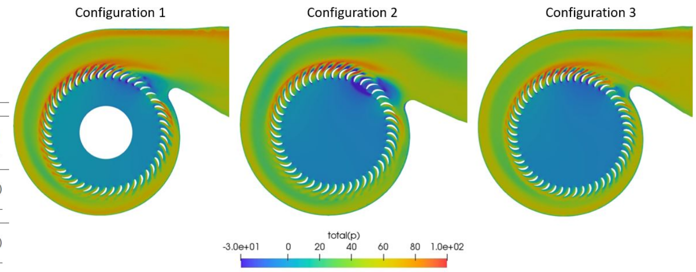

Fig. 7. Distribution of the total pressure (Pa) on plane 1 ($x = 0$, $y = 0$,$z = H_2/2$) for Configurations 1, 2 and 3.

separation is observed. The same mechanism is also observed in Configurations 2 and 3. For all configurations, a depression is observed in the trailing edge at the upper impeller region. The negative spot disappears gradually as the blades rotate, due to the advection of the trailing edge vortex.

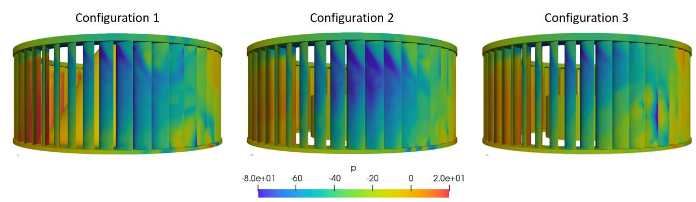

Fig. 8. Distribution of the static pressure P (Pa) on the impeller blades in a lateral view, for Configurations 1, 2 and 3.

In order to investigate the effect of the observed vortex on the flow around the blades, the parietal distribution of the static pressure on the impeller is presented in Fig.8. The impeller is oriented towards the volute exit. In Configurations 1 and 2, the flow is separated for multiple blades all along the height due to the strong interaction with the 3D vortex (Fig.7). However, in Configuration 3, the flow is separated along few blades, mostly in the tip region. As the flow is more attached along the blades in Configuration 3, the produced efficiency is higher.

C. Validation

As the SCF in Configuration 3 produced the best objective functions, a new experimental prototype was constructed. The static pressure and voluminal flowrate are quantified for the experimental prototype and compared to the numerical results. The SCF is connected to a pipe as in the computational domain (Fig.2). The diameter and length of the pipe are equal to 0.10 m and 0.92 m, respectively. The experimental procedure consists of measuring the generated flowrate by fixing the rotation speed of the fan and the pipe outlet pressure. The outlet pressure was controlled by varying the effective surface at the exit. The outlet pressure and velocity are measured by a manometer with an accuracy of $\pm 1\%$ and $\pm 3\%$, respectively.

Figure 9 represents the experimental and numerical values of the pressure drop Δp for different flowrates at a constant rotating speed of the fan (900 rpm). Δp is the average pressure difference between the outlet and the inlet. At the design point,

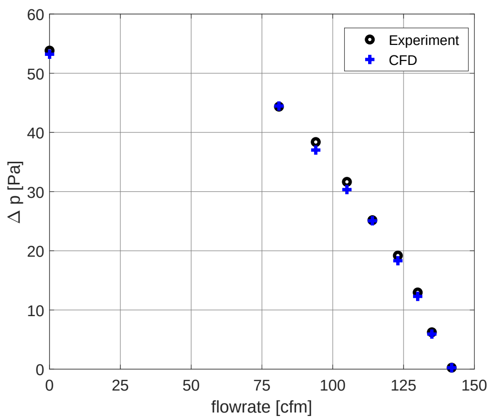

Fig. 9. Pressure drop Δp of the fan as a function of the voluminal flowrate.

a good agreement is observed between the simulated and the experimental data with a discrepancy of 3.4%. The maximum error between the numerical approach and the experimental results is 5.1% for 90 cfm.

V. Conclusion

This paper reported numerical results of the optimization process of an SCF, using opensource libraries. A complete automatic optimization loop was developed using Dakota, Salome for the geometry and mesh, and OpenFOAM for the numerical simulations. LHS and metamodels were selected to reduce the design points and expand the design space. Three configurations were tested with up to 7 design parameters.

The optimal design was obtained for Configuration 3 based on the EGO approach. By adding the two design parameters D_2 and R_c/D_2, the efficiency was improved by 4.1% compared to Configuration 2. Using a conical shape of the hub leads to a decrease and increase by 6% and 2% of the efficiency and F_{xy}, respectively. The distributions of the average velocity magnitude U showed the existence of a strong vortex between the cut-off and the impeller. The generated vortex leads to a total pressure decrease and forces the flow separation on the blades. The parietal static pressure confirmed the flow separation on multiple blades in Configurations 1 and 2. However, in Configuration 3, the separation region is mainly concentrated in the tip region.

Future works should integrate the variation of the blade profile along the span and the extension of the objective function by adding the radial forces and generated sound.

Acknowledgment

All calculations have been performed using the HPC facilities of the Compute Canada network, which is here gratefully acknowledged.

References

[1] R. Mokhtari and M. H. Jahangir, "The effect of occupant distribution on energy consumption and COVID-19 infection in buildings: A case study of university building," *Building and Environment*, vol. 190, p. 107561, 2021.

[2] K. Wang, Y. Ju, and C. Zhang, "Experimental and numerical investigations on effect of blade trimming on aerodynamic performance of squirrel cagefan," *International Journal of Mechanical Sciences*, vol. 177, p. 105579, 2020.

[3] F. P. Bleier, *Fan Handbook: Selection, Application, and Design*. New York: McGraw-Hill, 1997.

[4] R. J. Kind and M. G. Tobin, "Flow in a centrifugal fan of the squirrel-cage type," *Journal of Turbomachinery*, vol. 112, no. 1, pp. 84–90, 1990.

[5] R. Kind, "Prediction of flow behavior and performance of squirrel-cage centrifugal fans operating at medium and high flow rates," *Journal of Fluids Engineering*, vol. 119, no. 3, pp. 639–646, 1997.

[6] D. Raj and W. B. Swim, "Measurements of the mean flow velocity and velocity fluctuations at the exit of an FC centrifugal fan rotor," *Journal of Engineering for Gas Turbines and Power*, vol. 103, no. 2, pp. 393–399, 1981.

[7] S.-J. Seo and K.-Y. Kim, "Design optimization of forward-curved blades centrifugal fan with response surface method," ser. Proceedings of the ASME Heat Transfer/Fluids Engineering Summer Conference, vol. 2 A, Charlotte, North Carolina, USA, 01 2004, pp. 551–556.

[8] J. K. Kim and S. H. Kang, "Effects of the scroll on the flow field of a sirocco fan," ser. Proceedings of the ISROMAC-7, Hawai, 1997, pp. 1318–1327.

[9] S. Zhou, H. Zhou, K. Yang, H. Dong, and Z. Gao, "Research on blade design method of multi-blade centrifugal fan for building efficient ventilation based on Hicks-Henne function," *Sustainable Energy Technologies and Assessments*, vol. 43, p. 100971, 2021.

[10] S.-C. Lin and M.-L. Tsai, "An integrated performance analysis for a backward-inclined centrifugal fan," *Computers and Fluids*, vol. 56, pp. 24 – 38, 2012.

[11] M. Gholamian, G. K. M. Rao, and B. Panitapu, "Effect of axial gap between inlet nozzle and impeller on efficiency and flow pattern in centrifugal fans, numerical and experimental analysis," *Case Studies in Thermal Engineering*, vol. 1, no. 1, pp. 26 – 37, 2013.

[12] G. Angelini, T. Bonanni, A. Corsini, G. Delibra, L. Tieghi, and D. Volponi, "Optimization of an axial fan for air cooled condensers," *Energy Procedia*, vol. 126, pp. 754–761, 2017.

[13] V. D'Alessandro, S. Montelpare, R. Ricci, and A. Zoppi, "Numerical modeling of the flow over wind turbine airfoils by means of Spalart -Allmaras local correlation based transition model," *Energy*, vol. 130, pp. 402–419, 2017.

[14] F. Bothe, C. Friebe, M. Heinrich, and R. Schwarze, "CFD Simulation of Incompressible Turbomachinery A Comparison of Results From ANSYS Fluent and OpenFOAM," ser. Proceedings of ASME Turbo Expo: Power for Land, Sea, and Air, vol. 2B: Turbomachinery, Düsseldorf, Germany, 2014.

[15] F. R. Menter, "Two-equation eddy-viscosity turbulence models for engineering applications," *AIAA Journal*, vol. 32, no. 8, pp. 1598–1605, 1994.

[16] D. C. Wilcox, "Reassessment of the scale-determining equation for advanced turbulence models," *AIAA Journal*, vol. 26, no. 11, pp. 1299–1310, 1988.

[17] L. Daróczy, G. Janiga, K. Petrasch, M. Webner, and D. Thévenin, "Comparative analysis of turbulence models for the aerodynamic simulation of h-Darrieus rotors," *Energy*, vol. 90, pp. 680 – 690, 2015.

[18] M. Carnevale, F. Wang, and L. Di-Mare, "Calculation of Intake-Fan-Bypass Interaction With a Fan Similarity Model," ser. Proceedings of ASME Turbo Expo: Power for Land, Sea, and Air, vol. 2C: Turbomachinery, 2018.

[19] A. Theis, T. Reviol, and M. Böhle, "Analysis of the Losses in an Axial Fan With Small Blade Aspect Ratios Using CFD-Technique and Laser Doppler Anemometry," ser. Proceedings of ASME Turbo Expo: Power for Land, Sea, and Air, vol. 2A: Turbomachinery, Virtual, 2020.

[20] A. E. Benchikh Le Hocine, J. R. W. Lacey, and S. Poncet, "Turbulent flow over a D-section bluff body: a numerical benchmark," *Journal of Environmental Fluid Mechanics*, vol. 19, pp. 435–456, 2018.

[21] X. Wu, B. Liu, N. Ricks, and G. Ghorbaniasl, "Surrogate models for performance prediction of axial compressors using through-flow approach," *Energies*, vol. 13, no. 1, p. 169, 2019.

[22] D. Jones, M. Schonlau, and W. Welch, "Efficient global optimization of expensive black-box functions," *Journal of Global Optimization*, vol. 13, pp. 455–492, 12 1998.